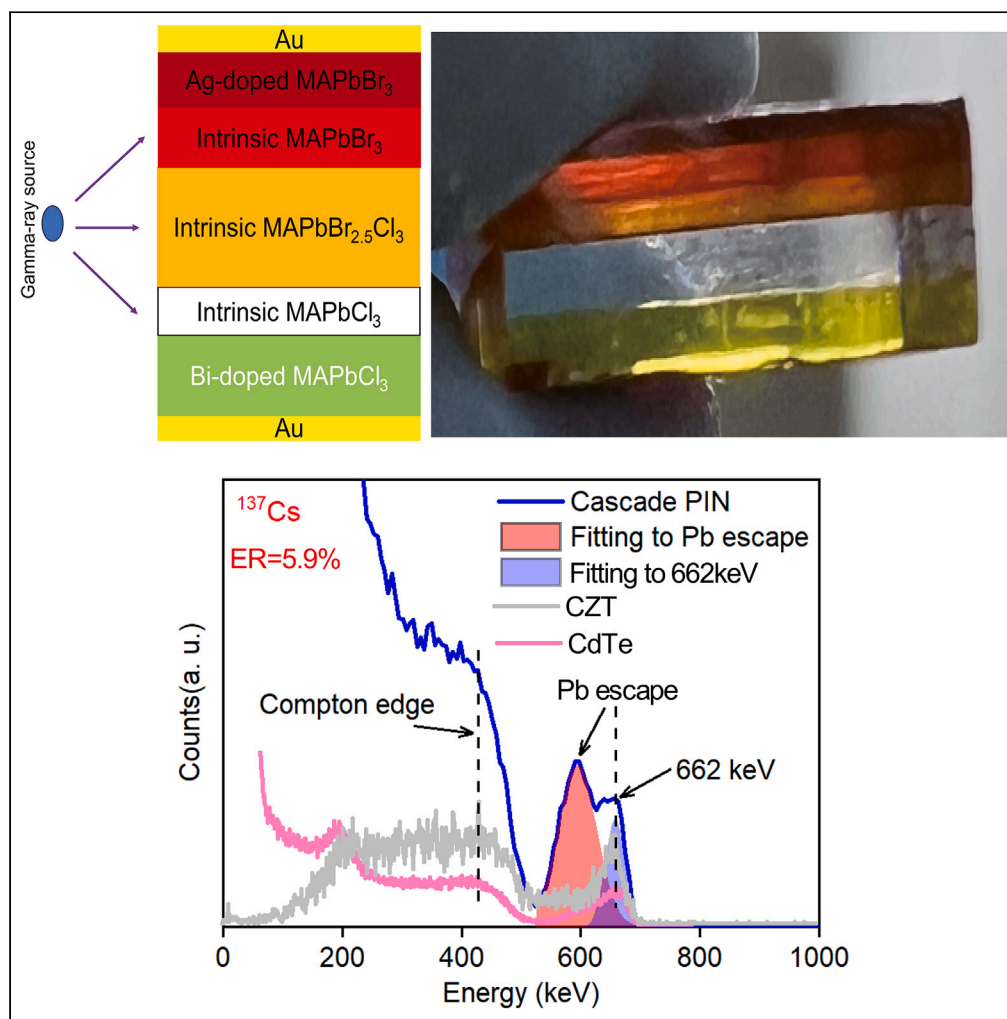


## Article

## Cascade perovskite single crystal for gamma-ray spectroscopy



Xin Wang, Yuzhu Pan, Yubing Xu, ..., Damian C. Onwudiwe, Xiaobao Xu, Wei Lei

xinw@seu.edu.cn (X.W.)  
xiaobaoxu@seu.edu.cn (X.X.)  
lw@seu.edu.cn (W.L.)

**Highlights**

Gamma-ray photodiodes made by solution-processed epitaxial growth

Fabrication of ion-formed electrical junctions in perovskite-based devices

Resolving gamma-ray photons based on solution-processed semiconductors

## Article

## Cascade perovskite single crystal for gamma-ray spectroscopy

Xin Wang,<sup>1,4,\*</sup> Yuzhu Pan,<sup>1</sup> Yubing Xu,<sup>1</sup> Jingda Zhao,<sup>1</sup> Yuwei Li,<sup>1</sup> Qing Li,<sup>1</sup> Jing Chen,<sup>1</sup> Zhiwei Zhao,<sup>1</sup> Xiaobing Zhang,<sup>1</sup> Byung Seong Bae,<sup>2</sup> Damian C. Onwudiwe,<sup>3</sup> Xiaobao Xu,<sup>1,\*</sup> and Wei Lei<sup>1,\*</sup>

## SUMMARY

The halide lead perovskite single crystals (HLPSCs) have great potential in gamma-ray detection with high attenuation coefficient, strong defects tolerance, and large mobility-lifetime product. However, mobile halide ions would migrate under high external bias, which would both weaken the gamma-ray response and cause additional noise. Here, we report the gamma-ray PIN photodiodes made of cascade HLPSCs including both ion-formed and electron-hole-formed electrical junctions that could suppress the ions migration and improve the charges collection. Our photodiodes based on cascade HLPSCs (MAPbBr<sub>3</sub>/MAPbBr<sub>2.5</sub>Cl<sub>0.5</sub>/MAPbCl<sub>3</sub>) show a wide halide-ion-formed depletion layer of ~52 μm. The built-in potential along the wide ionic-formed junction ensures a high mobility-lifetime product of  $1.1 \times 10^{-2} \text{ cm}^2\text{V}^{-1}$ . As a result, our gamma-ray PIN photodiodes exhibit compelling response to <sup>241</sup>Am, <sup>137</sup>Cs, and <sup>60</sup>Co; the energy resolution can reach 9.4%@59.5keV and 5.9%@662keV, respectively. This work provides a new path toward constructing high-performance gamma-ray detectors based on HLPSCs.

## INTRODUCTION

Gamma-ray detection by semiconductors and scintillation with large volume and high energy resolution has been widely used in medical applications, nuclear plant monitoring, and archaeology.<sup>1–3</sup> Due to the strong penetrating ability of gamma-ray photons, semiconductors for gamma-ray detection should consist of high Z elements, a millimeter-scale thickness, a large carrier mobility-lifetime product, a low defect density, and other strict criteria.<sup>4–7</sup>

Recently, halide lead perovskite single crystals (HLPSCs) have been thought of as next-generation room-temperature semiconductors for gamma-ray detection due to their high atomic number element, large carrier mobility-lifetime product, and strong defect tolerance values.<sup>8–10</sup> Since the first demonstration of using perovskite to sensing gamma rays, laudable attempts have been made to improve  $\mu\tau$  product including improving the single crystal quality (low trap density) and promote the resistivity.<sup>11</sup> Recently, a high  $\mu\tau$  product of  $8 \times 10^{-3} \text{ cm}^2\text{V}^{-1}$  has been reported in CsPbBr<sub>3</sub> HLPSCs from melt, which is approaching that of CdZnTe single crystals.<sup>7</sup> As a result, an energy resolution of 1.4% has been achieved for 662 keV gamma-ray photons. This result validates the superiority of HLPSC in detection of gamma-ray photons.

In general, as well as improving the quality of gamma-ray sensing single crystal by optimizing crystallization process or adding defect passivation ligand, constructing the heterojunction is an alternative and feasible approach to promote the  $\mu\tau$  product. Specifically, the formation of built-in potential at the heterojunction can efficiently reduce the leakage current by inhibiting the charge carrier recombination and consequently enhance the charge carrier lifetime for facilitating collection.<sup>12–15</sup> Thus, it is desired to form the heterojunction structure for obtaining  $\mu\tau$  product rather than only improving the quality of single crystals. It is worth noting that the intrinsic semiconductor character of perovskite can be easily regulated by modifying the component, whereas that of CdZnTe single crystals is hard due to unresolved growth issues.<sup>16–19</sup> To further explore and accomplish this advanced functionality, the structure of Au/perovskite/Au has been replaced by Au/perovskite/Sn to form efficient Schottky diode.<sup>8,20,21</sup> However, the metal electrodes would diffuse into perovskite and degenerate detection performance. As well, PIN diodes were also explored by deposit organic semiconductors (such as PTAA) and nanoparticles (such as ZnO, TiO<sub>2</sub>) as p-type and n-type layers.<sup>22–25</sup> However, the observation of additional noise can be assigned to the defects induced near the interface. In our previous work, we demonstrated the long charge carrier lifetime and low-noise PIN photodiode detector with Ag-doped MAPbBr<sub>3</sub> HLPSC and Bi-doped MAPbBr<sub>3</sub> HLPSC epitaxially grown on intrinsic MAPbBr<sub>2.5</sub>Cl<sub>0.5</sub> HLPSC, whereas the cascade architecture with gradient halide ion in perovskite single crystal also exhibits better charge carrier transporting.<sup>26–29</sup> All indicate the advantage of perovskite heterojunction for extracting high  $\mu\tau$  product and realizing sensitive gamma-ray detection.

<sup>1</sup>School of Electronic Science and Engineering, Joint International Research Laboratory of Information Display and Visualization, Southeast University, Nanjing, China

<sup>2</sup>Department of Electronics & Display Engineering, Hoseo University, Hoseo Ro 79, Asan City, Chungnam 31499, Korea

<sup>3</sup>Department of Chemistry, School of Mathematics and Physical Sciences, Faculty of Natural and Agricultural Sciences, North-West University, Mafikeng Campus, Private Bag X2046, Mmabatho 2735, South Africa

<sup>4</sup>Lead contact

\*Correspondence: xinw@seu.edu.cn (X.W.), xiaobaoxu@seu.edu.cn (X.X.), lw@seu.edu.cn (W.L.)

<https://doi.org/10.1016/j.isci.2023.107935>



In this work, we find that the halide ion interdiffusion length near the interfaces of cascade HLPSCs with a controlled halide gradient can reach tens of micrometers. Because of the large potential difference and width of the junction caused by the halide ion interdiffusion, we name this kind of junction “ion-formed electrical junction” to distinguish from normal electron-hole-formed electrical junction. These ion-formed electronic junctions positively influence charge transport and suppress ion migration. Assisted by epitaxial growth of high-quality doped HLPSC layers to form electron-hole-formed electronic junctions, a new structure of cascade HLPSC PIN photodiodes with electron-hole-formed electronic junctions and ion-formed electronic junctions is demonstrated with low noise and a large mobility-lifetime product. As a result, the delicate cascade architecture of MAPbCl<sub>3</sub>/MAPbBr<sub>2.5</sub>Cl<sub>0.5</sub>/MAPbCl<sub>3</sub> is designed as intrinsic layer. The gamma-ray PIN photodiode with cascade HLPSC as active layer shows the laudable performance of energy resolution toward distinguishing different isotopes, for example 9.4%@59.5keV and 5.9%@662keV for the <sup>241</sup>Am and <sup>137</sup>Cs, respectively.

## RESULTS AND DISCUSSION

Figure 1A depicts the schematic diagram of our proposed PIN photodiodes. Notably, the cascade HLPSC was used as the intrinsic layer. The cascade HLPSCs with different halide gradient were grown by solution-processed epitaxial growth. A high-quality N-type layer (Bi-doped MAPbCl<sub>3</sub>) and P-type layer (Ag-doped MAPbBr<sub>3</sub>) act as two lattice-matched functional layers.<sup>30–32</sup> More transport properties of the functional layers are shown in Figure S1. As shown in Figure 1B, the Bi-doped MAPbCl<sub>3</sub> layer can prevent the holes from injection, whereas the Ag-doped MAPbBr<sub>3</sub> can block the electrons from the cathode. In addition, the applied bias can be applied to the whole intrinsic layer with a length over the millimeter scale, which is beneficial for charge separation in gamma-ray detection.

To clarify the influence of heterojunction on  $\mu\tau$  product, cascade HLPSCs crystals with different halide gradients including 2-layer, 3-layer, and 4-layer were designed, as shown in Figure 1B. By using high-quality MAPbCl<sub>3</sub> HLPSC as substrates, cascade HLPSCs with different structures, including MAPbCl<sub>3</sub>/MAPbBr<sub>3</sub>, MAPbCl<sub>3</sub>/MAPbBr<sub>2.5</sub>Cl<sub>0.5</sub>/MAPbBr<sub>3</sub>, and MAPbCl<sub>3</sub>/MAPbBr<sub>1.5</sub>Cl<sub>1.5</sub>/MAPbBr<sub>2.5</sub>Cl<sub>0.5</sub>/MAPbBr<sub>3</sub>, are grown through solution-processed epitaxial growth (Figure S2). Cross-section photos of each cascade HLPSC are taken by scanning electron microscopy, as shown in Figure 1C. Because the lattice constant of MAPbCl<sub>3</sub> (5.668 Å) is smaller than that of the MAPbBr<sub>3</sub> (5.917 Å) single crystal and leads to a mismatch rate of 2.15%, an obvious interface is found between the two layers. By adding more transition layers that act as buffers, the interface becomes implicit. The lattice constant of each different HLPSC is measured by X-ray diffraction, as shown in Figure S3. To further reveal the quality of the interface between substrate and epitaxial growth layer, taking MAPbCl<sub>3</sub>/MAPbBr<sub>2.5</sub>Cl<sub>0.5</sub> heterojunction as example, high-resolution transmission electron microscopy is used, as shown in Figure 1D. Although some point defects exist near the interface, the lattice retains the same crystal orientation.

To confirm the halide gradient of each cascade HLPSC, the halide distribution is investigated through energy-dispersive X-ray (EDX) spectroscopy, as shown in Figures 1E–1G. The photoluminescence and time-resolved photoluminescence of each layer is shown in Figure S4, which agrees with previous work.<sup>15,33</sup> The results indicate the halide diffusion length depends on the halide ion gradient between the adjacent layers, which is in accordance with previous work. The larger the halide gradient between the adjacent layers is, the longer the halide diffusion length becomes, for example, the halide interdiffusion length between the MAPbCl<sub>3</sub>/MAPbBr<sub>3</sub> heterojunction is approximately 38  $\mu\text{m}$  (Figure 1E), whereas the halide interdiffusion length between MAPbCl<sub>3</sub>/MAPbBr<sub>2.5</sub>Cl<sub>1.5</sub> and MAPbBr<sub>2.5</sub>Cl<sub>0.5</sub>/MAPbBr<sub>3</sub> reaches only approximately 22 and 18  $\mu\text{m}$  (Figure 1F), respectively. For the 4-layer cascade HLPSC, the interdiffusion lengths between MAPbCl<sub>3</sub>/MAPbBr<sub>1.5</sub>Cl<sub>1.5</sub> and MAPbBr<sub>1.5</sub>Cl<sub>1.5</sub>/MAPbBr<sub>2.5</sub>Cl<sub>0.5</sub> are only 11 and 18  $\mu\text{m}$ , respectively, as shown in Figure 1G. As a result, a large halide gradient is beneficial for a longer interdiffusion length, but the large halide gradient may sacrifice the lattice mismatch rate, which can result in a high density of defects.

It is well known that the ion diffusion along the component gradient is inevitable, especially the halide ion in perovskites due to the low activation energy in soft lattice. Also, the published result demonstrates the halide ion diffusivity of  $10^{-10}\sim 10^{-13}\text{cm}^2\text{s}^{-1}$  around 80–100°C in CsPbCl<sub>3</sub>/CsPbBr<sub>3</sub> perovskite.<sup>34,35</sup> To investigate the stability of the halide gradient in cascade HLPSCs, a 2-layer cascade HLPSC with the structure of MAPbCl<sub>3</sub>/MAPbBr<sub>3</sub> was heated at 75°C in air for 8, 120, and 1000 h. It was surprising that the width of the transition layer remains nearly 38  $\mu\text{m}$ , as shown in Figure 1H. This result indicates the halide ion diffusion could reach equilibrium and then almost stop, which confirms halide gradient in our as-fabricated cascade HLPSCs maintaining good stability.

To roughly find the most suitable halide gradient for cascade HLPSCs, the  $\mu\tau$  product is roughly measured through the photocurrent under various biases to the modified Hecht equation (experimental setup is shown in Figure S5). For an individual MAPbBr<sub>2.5</sub>Cl<sub>0.5</sub> HLPSC, as shown in Figure 2A, the  $\mu\tau$  product is measured as  $0.3 \times 10^{-3}\text{cm}^2\text{V}^{-1}$ . The 2-layer cascade HLPSC shows a relatively large  $\mu\tau$  product of  $1.42 \times 10^{-3}\text{cm}^2\text{V}^{-1}$ , as shown in Figure 2B. The 3-layer cascade HLPSC shows the highest charge collection efficiency and the largest  $\mu\tau$  product of  $5.2 \times 10^{-3}\text{cm}^2\text{V}^{-1}$ , which is nearly 14 times larger than that of the individual MAPbBr<sub>2.5</sub>Cl<sub>0.5</sub> HLPSC (Figure 2C). However, when crossing the 4-layer cascade HLPSC (Figure 2D), the  $\mu\tau$  product decreases to  $1.52 \times 10^{-3}\text{cm}^2\text{V}^{-1}$ .

In addition, the current density (J)–voltage (V) hysteresis of different cascade HLPSCs is investigated to examine ion migration. The individual MAPbBr<sub>2.5</sub>Cl<sub>0.5</sub> HLPSC shows the largest J–V hysteresis (Figure 2E). It is obvious that the heterojunction made by the 2-layer HLPSC can suppress J–V hysteresis (Figure 2F), and the 3-layer cascade HLPSC (Figure 2G) is nearly hysteresis-free, which indicates that halide ion migration comes across some unexpected barriers in cascade HLPSCs. When the cascade HLPSC is made of 4 layers, the hysteresis worsens (Figure 2H). Considering that the number of layers in cascade HLPSCs will not largely affect the crystallization quality, the large  $\mu\tau$  product and hysteresis-free cascade HLPSCs can be attributed to the ion-formed electrical junction sustain almost all the bias and the halide ions cannot migrate during the ion-formed electrical junction. More information about built-in electrical field of ion-formed electrical junction is explained in Figure S6.

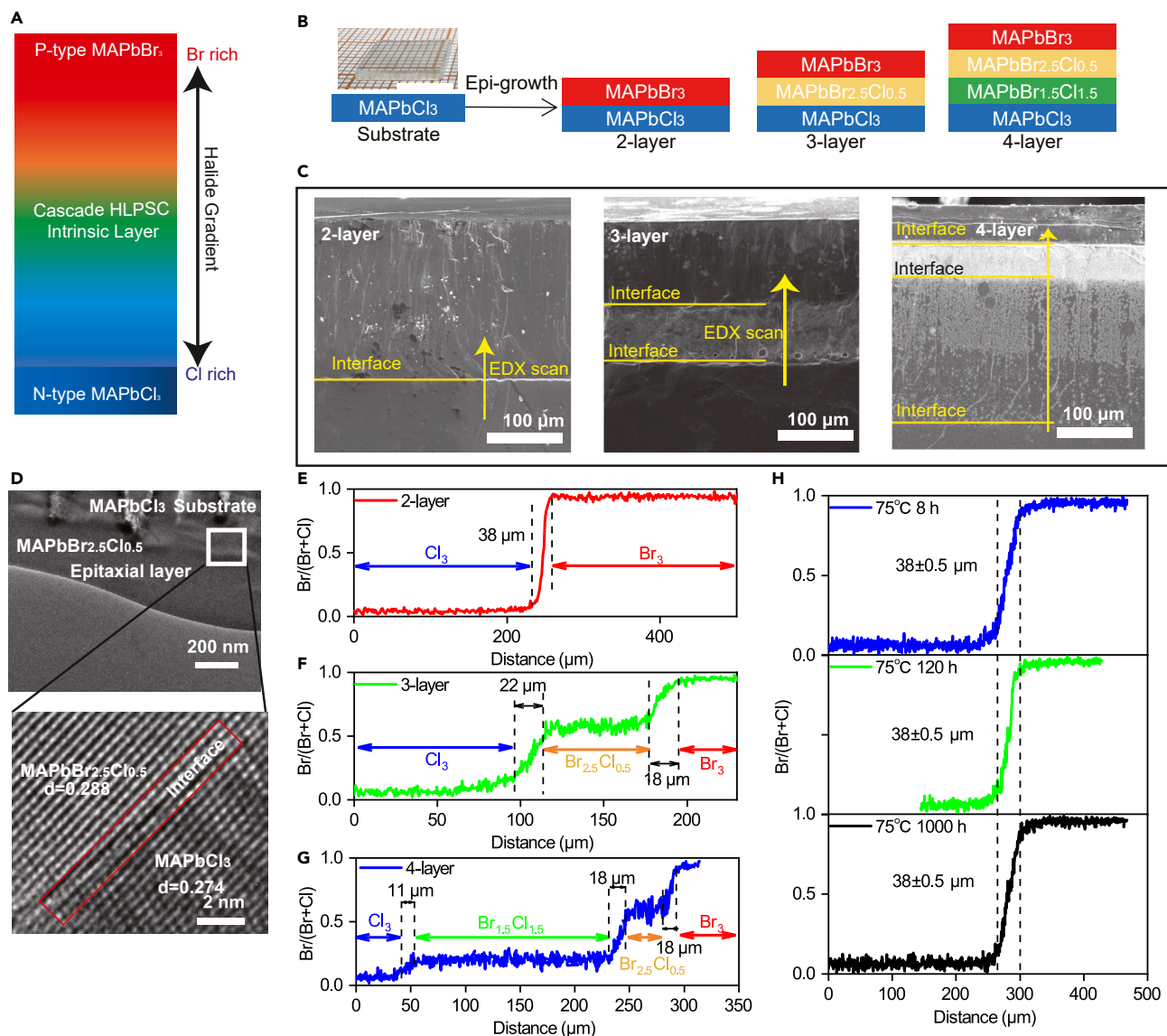


**Figure 1. Characterization of the cascade HLPSC with different halide gradients**

(A) Device structure of the cascade HLPSC PIN photodiode.

(B) Epitaxial growth of the cascade HLPSC with different halide gradients.

(C) Cross-section of the cascade HLPSCs: MAPbCl<sub>3</sub>/MAPbBr<sub>3</sub> (left), MAPbCl<sub>3</sub>/MAPbBr<sub>2.5</sub>Cl<sub>0.5</sub>/MAPbBr<sub>3</sub> (middle) and MAPbCl<sub>3</sub>/MAPbBr<sub>1.5</sub>Cl<sub>1.5</sub>/MAPbBr<sub>2.5</sub>Cl<sub>0.5</sub>/MAPbBr<sub>3</sub> (right).

(D) TEM photo of the interfaces near the MAPbCl<sub>3</sub>/MAPbBr<sub>2.5</sub>Cl<sub>0.5</sub> heterojunction fabricated by FIB (top); high-resolution TEM photo of the interfaces.

(E) Line scan of the cascade HLPSC through energy-dispersive X-rays for MAPbCl<sub>3</sub>/MAPbBr<sub>3</sub>.

(F) MAPbCl<sub>3</sub>/MAPbBr<sub>2.5</sub>Cl<sub>0.5</sub>/MAPbBr<sub>3</sub>.

(G) MAPbCl<sub>3</sub>/MAPbBr<sub>1.5</sub>Cl<sub>1.5</sub>/MAPbBr<sub>2.5</sub>Cl<sub>0.5</sub>/MAPbBr<sub>3</sub>.

(H) Br-Cl interdiffusion length in MAPbCl<sub>3</sub>/MAPbBr<sub>3</sub> after different times.

To understand why the halide gradient in cascade HLPSCs can suppress halide migration in different layers and how the halide gradients in cascade HLPSCs enhance charge transport and to extract the details at heterojunction, Kelvin probe force microscope (KPFM) was employed to measure the built-in potential along the cross-section of cascade HLPSCs.<sup>36</sup> Figure 3A displays the schematic diagram of measurement. An infrared laser was focused on the tip of the magnetic probe. When the tips scan across the cascade HLPSCs, they will exhibit different vibrations because the potential changes, and the tiny vibration of the tips will be grasped by an infrared detector. As shown in Figure 3B, the potential decreases from 4.68 V of MAPbCl<sub>3</sub> to 4.60 V of MAPb<sub>1.5</sub>Cl<sub>1.5</sub>, with 0.08 V potential difference at the heterojunction of MAPbCl<sub>3</sub>/MAPbBr<sub>1.5</sub>Cl<sub>1.5</sub>. The width of depletion region is 8 μm, which is approaching to the ion diffusion length of 11 μm (see Figure 1G). Meanwhile,

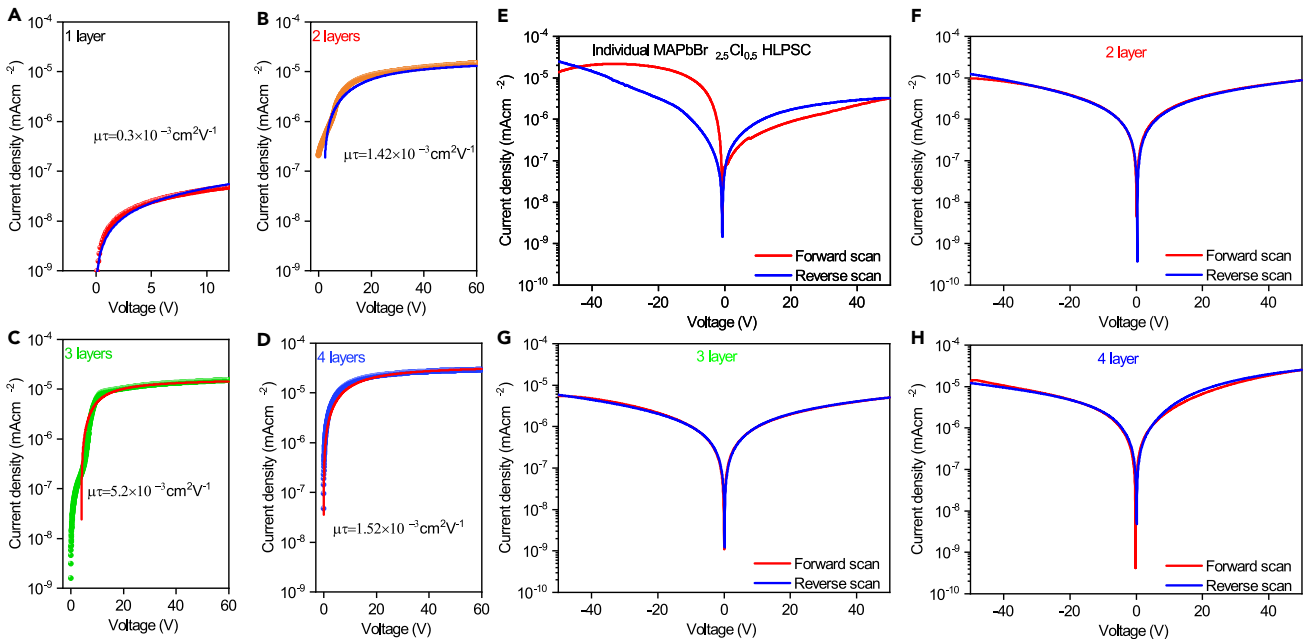


**Figure 2. Mobility-lifetime product and hysteresis of cascade HLPSCs with different halide gradients**

(A–D) Photocurrent density versus voltage curves. (A) Individual MAPbBr<sub>2.5</sub>Cl<sub>0.5</sub> HLPSC. (B) 2-layer. (C) 3-layer. (D) 4-layer.

(E–H) I–V curves of the cascade HLPSCs with different halide gradients at the forward scan (red) and reverse scan (blue). (E) Individual MAPbBr<sub>2.5</sub>Cl<sub>0.5</sub> HLPSC. (F) 2-layer. (G) 3-layer. (H) 4-layer.

the potential difference was found to be 0.362, 0.365, and 0.101 V with the depleted width of 24, 15, 18, and 28 μm for MAPbCl<sub>3</sub>/MAPbBr<sub>2.5</sub>Cl<sub>0.5</sub> (Figure 3C), MAPbCl<sub>3</sub>/MAPbBr<sub>3</sub> (Figure 3D), MAPbBr<sub>1.5</sub>Cl<sub>1.5</sub>/MAPbBr<sub>2.5</sub>Cl<sub>0.5</sub> (Figure 3E), and MAPbBr<sub>2.5</sub>Cl<sub>0.5</sub>/MAPbBr<sub>3</sub> (Figure 3F) heterojunction, respectively. The wide depletion area makes it suitable for efficient charges collection generated from gamma-ray photons.

It is worth noting that the variation of potential difference at the heterojunction follows the similar tendency to that of halide ion diffusion length, in which variation depends on the difference of halide ion gradient. To clarify the influence of ion diffusion and electron-hole concentration, we measured the charges density with Hall field. Here, the charge density measured from the Hall field is shown in Figure 3G, and the charge density of the intrinsic MAPbBr<sub>x</sub>Cl<sub>(3-x)</sub> HLPSC is 10<sup>9</sup>–10<sup>11</sup> cm<sup>-3</sup>. Unfortunately, the charge density cannot support such a large electron barrier in the heterojunctions. As calculated by equation  $V_{bi} = 0.0259 \ln \left( \frac{N_a N_d}{n_i^2} \right)$ ,  $N_a$  is  $8 \times 10^9 \text{ cm}^{-3}$  and  $6 \times 10^{10} \text{ cm}^{-3}$  for MAPbBr<sub>2.5</sub>Cl<sub>0.5</sub> and MAPbBr<sub>3</sub>, respectively.  $N_d$  is  $1 \times 10^{11} \text{ cm}^{-3}$  and  $3 \times 10^{10} \text{ cm}^{-3}$  for MAPbCl<sub>3</sub> and MAPbBr<sub>1.5</sub>Cl<sub>1.5</sub>, respectively.  $n_i$  is  $10^{10} \text{ cm}^{-3}$ <sup>37</sup>; the energy barrier should be nearly 0.1, 0.08, and 0.05 eV for MAPbCl<sub>3</sub>/MAPbBr<sub>3</sub>, MAPbCl<sub>3</sub>/MAPbBr<sub>2.5</sub>Cl<sub>0.5</sub>, and MAPbBr<sub>1.5</sub>Cl<sub>1.5</sub>/MAPbBr<sub>2.5</sub>Cl<sub>0.5</sub> heterojunctions, respectively. This result is much smaller than the potential difference measured from KPFM results, which means the charge density could not support such large potential difference at the heterojunctions. It is deduced that the halide ion diffusion also makes non-negligible contribution to the potential difference at heterojunction. The band structure of individual HLPSCs is shown in Figure S7.

Compared with the normal p-n junction, for the (n-type MAPbCl<sub>3</sub>)/MAPbCl<sub>3</sub>, (p-type MAPbBr<sub>3</sub>)/MAPbBr<sub>3</sub>, and (n-type MAPbBr<sub>3</sub>)/MAPbBr<sub>3</sub> homojunctions (Figure S8), the electron-hole-formed electronic junction reaches 0.40, 0.13, and 0.35 V, whereas the widths are only 0.74, 0.31, and 0.61 μm, respectively. This finding indicates that the ion-formed electronic junction in cascade HLPSCs shows a much wider charge depletion layer than normal electronic junctions, which is more beneficial for high-energy photon detection.

Based on the KFM experiments, the band structure of each cascade HLPSC with different halide gradients is described in Figures 3F–3J. The band gap is measured from the absorption curve (Figure S9). In the cascade HLPSC with structure of MAPbCl<sub>3</sub>/MAPbBr<sub>2.5</sub>Cl<sub>0.5</sub>/MAPbBr<sub>3</sub>, the total depleted region reaches 52 μm and built-in potential achieves 0.463 V. This wide depleted region and large potential difference would separate and drift the electron-hole pairs, which is more beneficial for sensing high-energy gamma-ray photons. Thus, the 3-layer cascade HLPSC was selected as candidate intrinsic layer for gamma-ray PIN photodiodes.

To further study the carrier dynamics in this 3-layer cascade HLPSC, three types of electron-only, hole-only, and full devices were fabricated. And the setup of the experiments is shown in Figure S10. As shown in Figure 4A, Bi-doped MAPbBr<sub>3</sub> (0.1 mm) and Bi-doped-MAPbCl<sub>3</sub> HLPSCs (2 mm) were used as electron selective transport layers (n-type), whereas 3-layer cascade HLPSC (0.6, 1.7, and 0.6 mm) acts as an intrinsic layer. The high voltage bias is applied on the Bi-doped MAPbCl<sub>3</sub>. Under the irradiation of alpha (α) particle with energy of 5.4 MeV from <sup>241</sup>Am, the electron-hole pairs would be generated. Since the two n-type layers would form energy barriers and block the holes, only electron can transport across the whole device and then was collected at external circuit. Likewise, only holes go through the whole

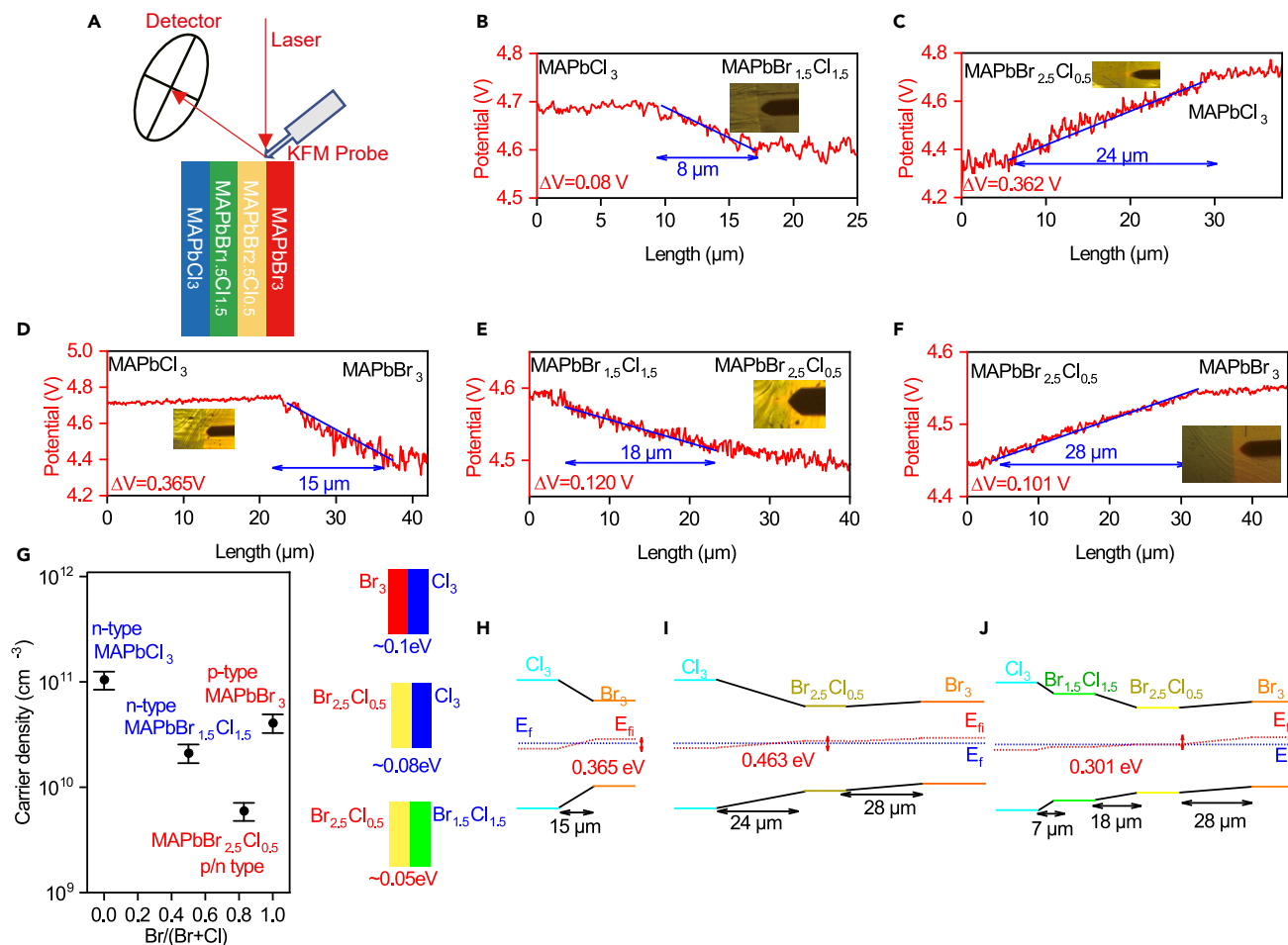


**Figure 3. Transport properties of the cascade HLPSCs with different halide gradients**

- (A) Diagrammatic sketch of the Kelvin-force microscope experiments.
- (B) Energy structure of the MAPbCl<sub>3</sub>/MAPbBr<sub>1.5</sub>Cl<sub>1.5</sub> heterojunction.
- (C) Energy structure of the MAPbCl<sub>3</sub>/MAPbBr<sub>2.5</sub>Cl<sub>0.5</sub> heterojunction.
- (D) Energy structure of the MAPbCl<sub>3</sub>/MAPbBr<sub>3</sub> heterojunction.
- (E) Energy structure of the MAPbBr<sub>1.5</sub>Cl<sub>1.5</sub>/MAPbBr<sub>2.5</sub>Cl<sub>0.5</sub> heterojunction.
- (F) Energy structure of the MAPbBr<sub>2.5</sub>Cl<sub>0.5</sub>/MAPbBr<sub>3</sub> heterojunction.
- (G) Carrier densities of HLPSCs with different halide components via the Hall effect and the energy barrier calculated from the carrier density.
- (H) Energy structure of the 2-layer cascade HLPSC.
- (I) Energy structure of the 3-layer cascade HLPSC.
- (J) Energy structure of the 4-layer cascade HLPSC.

device of n-type MAPbBr<sub>3</sub>/cascade HLPSCs (thickness 0.1, 1.1, 1.0, 0.26 mm) under bias (Figure 4B). Figure 4C presents the full PIN photodiode device through solution-processed epitaxial growth with Bi-doped MAPbCl<sub>3</sub> and Ag-doped MAPbBr<sub>3</sub> as n-type and p-type layers, respectively.

Through directly tracing the pulse signal from the preamplifier through an oscilloscope, the response time for electrons from electron-only device (Figure 4A) and holes from hole-only device (Figure 4B) under different applied voltage are shown in Figures 4D and 4E. According to the equation  $\tau = \frac{\mu}{\sigma}V^{-1}$ , the average electron mobility and hole mobility were fitted as 442.4 cm<sup>2</sup>V<sup>-1</sup>s<sup>-1</sup> (Figure 3F) and 294.5 cm<sup>2</sup>V<sup>-1</sup>s<sup>-1</sup> (Figure 3G), respectively. For the comparison, the time-of-flight experiments were also conducted with 7 ns laser (Figure S11), giving a similar result. As well, in the full p-i-n device, the nuclide of <sup>241</sup>Am was put at the side face of the device. And the 5.5 MeV alpha particles will directly incident into the intrinsic layer. To figure out the largest charges collection efficiency, we controlled the voltage bias from 50 to 500 V. The signal of 5.5 MeV <sup>241</sup>Am was extracted from voltage-dependent spectrums, as shown in Figure 4H. By fitting the peak positions to Hecht equation, the  $\mu\tau$  product is extracted as 1.1 × 10<sup>-2</sup> cm<sup>2</sup>V<sup>-1</sup> (Figure 4I), which is comparable with the best reported single HLPSC including CsPbBr<sub>3</sub> grown using Bridgeman's method and FA<sub>0.9</sub>Cs<sub>0.1</sub>PbBr<sub>3</sub> grown from solutions.<sup>7,38</sup>

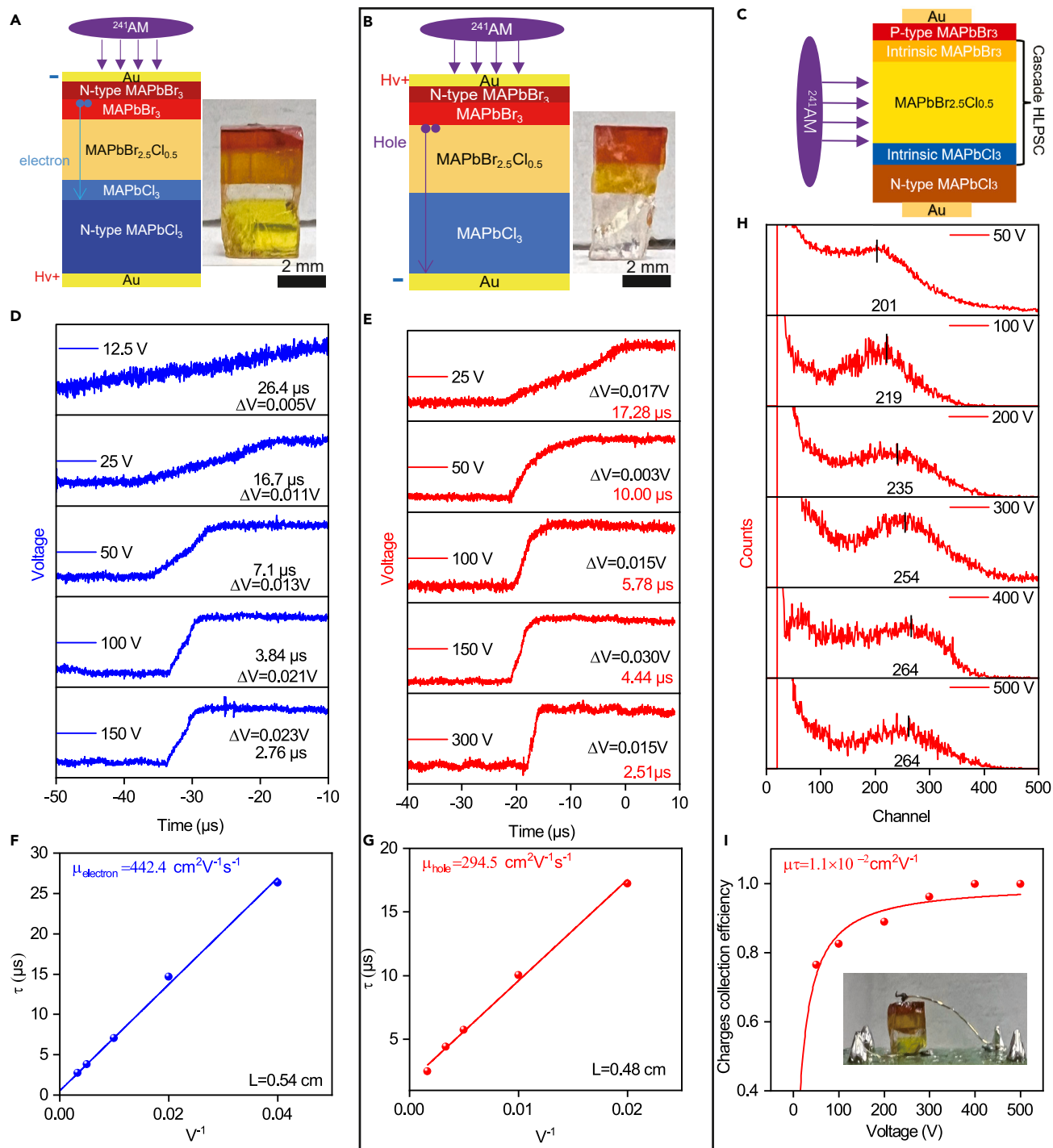


**Figure 4. Optoelectronic properties of the 3-layer cascade HLPSC measured by alpha particles from <sup>241</sup>Am**

(A) N-I-N-type photodiode made of a 3-layer cascade HLPSC.

(B) N-I-I-type photodiode made of a 3-layer cascade HLPSC.

(C) P-I-N-type photodiode made of a 3-layer cascade HLPSC.

(D) Response time of N-I-N-type photodiodes under various biases under alpha particles from <sup>241</sup>Am to measure electron mobility.

(E) Response time of N-I-I-type photodiodes under various biases under alpha particles from <sup>241</sup>Am to measure hole mobility.

**Figure 4. Continued**

(F) Electron mobility of the 3-layer cascade HLPSC.

(G) Hole mobility of the 3-layer cascade HLPSC.

(H) Voltage-dependent spectra of 5.5 MeV alpha particles detected from P-I-N-type photodiodes.

(I) Charge mobility-lifetime product fitting to the Hecht equation.

Figure S12 presents the J-V curve of full PIN photodiode device toward visible photons and under dark. The device presented a good rectification and showed a low dark current of  $\sim 9 \text{ nAcm}^{-2}$  even under  $-150 \text{ V}$ , which confirms our device can efficiently suppress the leakage current. More importantly, the photocurrent density is 4 times larger than that of HPSC PIN photodiode with individual single crystal as intrinsic layer (Figure S13). The boost of photocurrent is believed to result from the larger  $\mu\tau$  product and wider depletion region with cascade HLPSC as intrinsic layer in PIN photodiodes.

Because we have confirmed the advantage of cascade HLPSCs for constructing p-i-n device with large  $\mu\tau$  product, to further utilize this advanced functionality, we further evaluate its detection performance toward series isotopes. As shown in Figure 5A, during gamma-ray detection, the gamma-ray photodiodes are placed inside a copper box to avoid electromagnetic interference and visible light. Then, a high voltage is applied to the photodiodes to collect photo-induced charges. To discriminate the weak signal generated from gamma-ray photons, a preamplifier (CR-110 from CREMAT, USA) is used to amplify the charges, and a shaping amplifier (CR-210 for baseline restorer and CR-200 for shaping from CREMAT, USA) is used to integrate the pulse into Gaussian shaping. At this point, the photon signal can be converted to a 0–5 V Gaussian pulse and collected in a multiple-channel analyzer (APG7300A from AP, Japan). When  $^{137}\text{Cs}$  is close to the gamma-ray photodiode, typical photon peaks are shown in Figure 5B. Thus, two obvious peaks are captured in a duration of nearly 20 ms. Figure 5C shows the typical photon peaks shaped by the shaping amplifier with different shaping times. Benefit from the fast response speed of our cascade HLPSC-based PIN photodiode, shaping time of both 1  $\mu\text{s}$  and 8  $\mu\text{s}$  could integrate the charges in one Gaussian pulse (Figure 5C), and output signal is large enough to discriminate from the noise when compared with using individual HLPSC in PIN photodiode (Figure S14).

The  $^{241}\text{Am}$  gamma-ray spectrum resolved by the cascade HLPSC PIN photodiode under a bias of 300 V is shown in Figure 5D. Because  $^{241}\text{Am}$  radiates 59.5 keV gamma-ray photons and 5.4 MeV alpha particles simultaneously, two peaks are found in the gamma-ray spectrum. The energy resolution for 59.5 keV gamma-ray photons is 9.4%. The energy resolution for 5.4 MeV alpha particles is 21.9%. And the response to only 59.5 keV under different bias is shown in Figure S15.

For the  $^{137}\text{Cs}$  662 keV gamma-ray photons, we use high-quality CdTe (300 V) and CdZnTe (3000 V) for calibration. The Pb escape peak is detected, whereas the energy resolution is 5.9%@662keV for the cascade HLPSC PIN photodiodes at 300 V (Figure S6E). In addition,  $^{60}\text{Co}$  with 1173 keV and 1333 keV gamma-ray photons is detected by the cascade HLPSC PIN photodiodes at 300 V (Figure 5F). However, because the thickness of the cascade HLPSC PIN photodiode is only 0.54 cm, most photons with energy over 1 MeV transmit the device without response. Thus, it is safe to say the photopeak of  $^{60}\text{Co}$  can be detected, but we cannot provide the value of creditable energy resolution. Besides, for 662keV gamma-ray photons, the largest channel number is nearly 27 mV (channel number 109/4096) and 49 mV (channel number 202/4096) after preamplifier for 662 keV and 1173 keV, respectively. Thus, the charge quantity is then estimated to be 19 fC and 35 fC for 662 keV and 1173 keV gamma-ray photons, respectively. Consider the excite energy is nearly 6 eV; 1,10,000 and 1,95,500 electron-hole pairs should be activated. Thus, the activated charges should be 35.2 and 62.5 fC for 662 keV and 1173 keV, respectively. And the charges collection efficiency is 54% and 56% for 662keV and 1173keV, respectively. Comparisons of our cascade HLPSC PIN photodiodes are shown in Table S1.

In addition, because the ion-formed electrical field can suppress ion migration, this cascade HLPSC PIN photodiode demonstrates no poor stable response over time, as shown in Figure 5G. Over a continuous period of 15 min, the channel number of the peak for  $^{137}\text{Cs}$  does not change, which indicates that the photo response or electrical field is not weakened due to halide ion migration under bias. Besides,  $^{137}\text{Cs}$  spectrums acquired from different cascade HLPSC PIN photodiode samples are shown in Figure S16.

In conclusion, ion-formed and electron-hole-formed electronic junctions are established in cascade HLPSC PIN photodiodes. Due to the ion-formed electronic junction, ion migration can be suppressed, and the charge collection efficiency can be increased. Our cascade HLPSC PIN photodiodes show low noise and a large response to gamma-ray photons; in addition, they can distinguish different isotopes through the gamma-ray spectrum. Our work provides a new path toward high-energy-resolution gamma-ray photodiodes based on solution-processed single crystals.

**Limitation of the study**

At this stage, the stability of the cascade HLPSC is good. However, the electrodes are not stable after long-term high bias. During experiments, the Au wire may scratch the electrodes during connection. Besides, The Au electrode will fail after long time high bias (over 48 h, 600 V). Two approaches may improve the situation: one is to add a buffer layer between the p-type layer and electrode; another method is to improve the method of bonding. We are still working on this issue.

**STAR★METHODS**

Detailed methods are provided in the online version of this paper and include the following:

- KEY RESOURCES TABLE

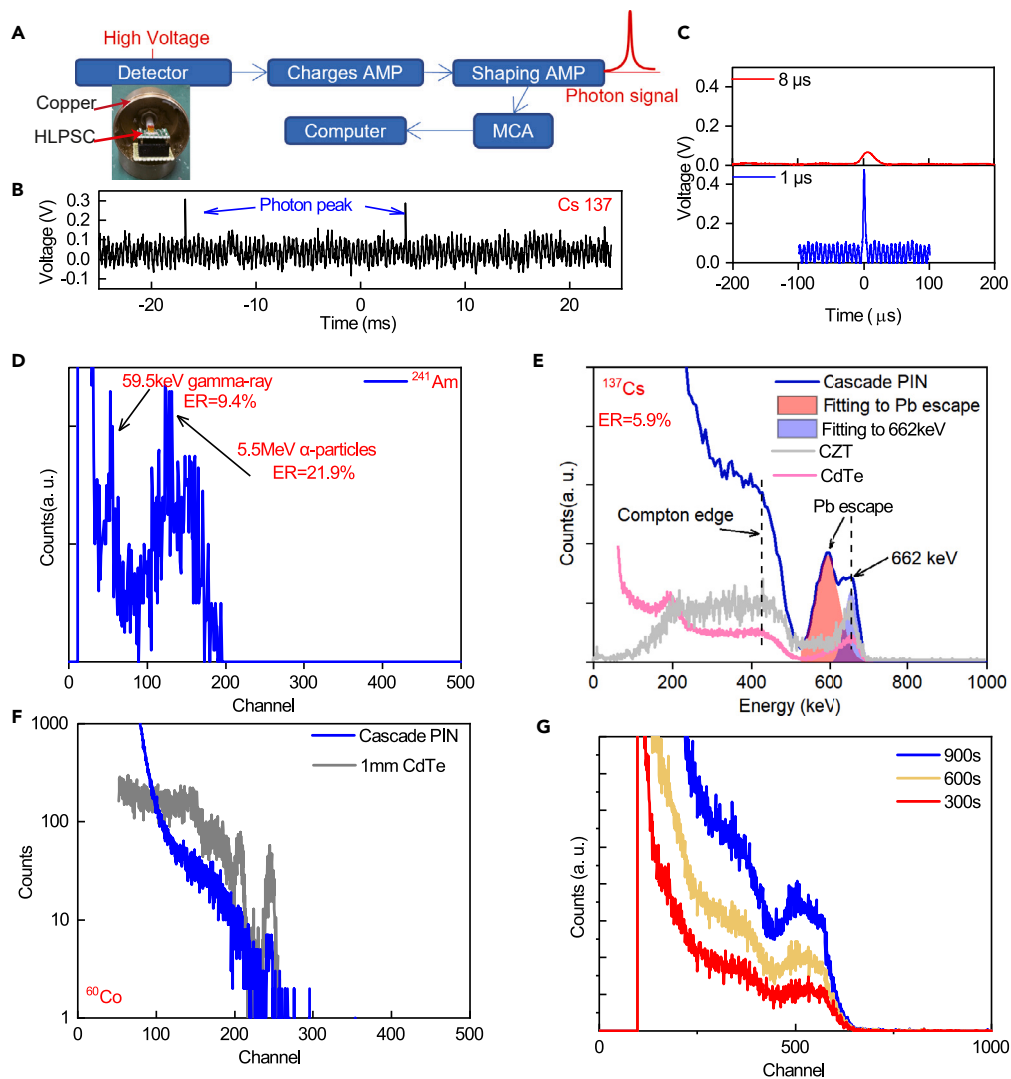


**Figure 5. Gamma-ray response of the cascade HLPSC PIN photodiode to different isotopes**

- (A) Setup of the experiments.  
 (B) Response to gamma-ray photons captured by the oscilloscope.  
 (C) Single-photon peak generated by  $^{137}\text{Cs}$  in the cascade HLPSC PIN photodiode with different shaping times.  
 (D) Energy-resolved spectrum by the cascade HLPSC PIN photodiode under  $^{241}\text{Am}$  by using a shaping time of  $8\ \mu\text{s}$ .  
 (E) Energy-resolved spectrum by the cascade HLPSC PIN photodiode under  $^{137}\text{Cs}$  662 keV  $\gamma$ -ray by using a shaping time of  $8\ \mu\text{s}$ .  
 (F) Energy-resolved spectrum by the cascade HLPSC PIN photodiode under the  $^{60}\text{Co}$  1173 keV  $\gamma$ -ray.  
 (G) Stability of the spectrum of the cascade HLPSC PIN photodiode over a period of 15 min under  $^{137}\text{Cs}$ .

● **RESOURCE AVAILABILITY**

- Lead contact
- Materials availability
- Data and code availability

● **METHODS DETAILS**

- Growth of the cascade HLPSC PIN photodiodes
- Characterization of the HLPSC and photodiodes
- Experiments of the gamma-ray photodiodes

● **QUANTIFICATION AND STATISTICAL ANALYSIS**

## SUPPLEMENTAL INFORMATION

Supplemental information can be found online at <https://doi.org/10.1016/j.isci.2023.107935>.

## ACKNOWLEDGMENTS

This work is financially supported by National Natural Science Foundation Project for Young Researcher (12005038, 12375306), China Postdoctoral Foundation funded project (2023T160106, 2023M730555), National Key Research and Development Program of China (2021YFE0105900, 2022YFE0139100), National Natural Science Foundation Project of China (62175028, 51879042, 61674029), Program 111\_2.0 in China (BP0719013), Leading Technology of Jiangsu Basic Research Plan (BK20192003), and International cooperative research project of Jiangsu province (BZ2022008).

## AUTHOR CONTRIBUTIONS

X.W. and W. L. conceived the work. X.W., Y.P., and Y.X. grow the cascade HLPSC. X.W., J.Z., Y.L., and Q.L. performed the chemical synthesis. X.W., J.C., and Z.Z. performed the SEM and energy dispersive X-ray measurements. X.W., X.Z., and B.B. performed the X-ray diffraction. X.W., O.D., and X.X. performed the gamma-ray detection experiments. X.W., X.X., and W.L. wrote the manuscript. All the authors contributed to the work and commented on the paper.

## DECLARATION OF INTERESTS

The authors declare no competing interests.

Received: June 2, 2023

Revised: July 19, 2023

Accepted: September 13, 2023

Published: September 20, 2023

## REFERENCES

- Baussens, O., Montémont, G., Verilhac, J.M., Hirsch, L., and Gros-Daillon, E. (2022). Noise spectroscopy study of methylammonium lead tribromide single-crystal detectors: Gamma-ray spectroscopy applications. *Nucl. Instrum. Methods Phys. Res.* 1038. <https://doi.org/10.1016/j.nima.2022.166904>.
- Gao, L., Sun, J.L., Li, Q., and Yan, Q. (2022). gamma-ray Radiation Hardness of CsPbBr<sub>3</sub>(3) Single Crystals and Single-Carrier Devices. *ACS Appl. Mater. Interfaces* 14, 37904–37915. <https://doi.org/10.1021/acsmi.2c08471>.
- Yakunin, S., Dirin, D.N., Shynkarenko, Y., Morad, V., Cherniukh, I., Nazarenko, O., Kreil, D., Nauser, T., and Kovalenko, M.V. (2016). Detection of gamma photons using solution-grown single crystals of hybrid lead halide perovskites. *Nat. Photonics* 10, 585–589. <https://doi.org/10.1038/nphoton.2016.139>.
- Pan, L., Liu, Z., Welton, C., Klepov, V.V., Peters, J.A., De Siena, M.C., Benadia, A., Pandey, I., Miceli, A., Chung, D.Y., et al. (2023). Ultra-High Flux X-Ray Detection by Solution-Grown Perovskite CsPbBr<sub>3</sub>(3) Single Crystal Semiconductor Detector. *Adv. Mater.* 35, e2211840. <https://doi.org/10.1002/adma.202211840>.
- Pan, L., He, Y., Klepov, V.V., De Siena, M.C., and Kanatzidis, M.G. (2022). Perovskite CsPbBr<sub>3</sub>(3) Single Crystal Detector for High Flux X-Ray Photon Counting. *IEEE Trans. Med. Imag.* 41, 3053–3061. <https://doi.org/10.1109/TMI.2022.3176801>.
- Xu, Q., Lu, J., Hu, J., Ge, Z., Zhu, D., Bi, Y., Wang, J., and Ouyang, X. (2020). CsPbBr<sub>3</sub> Single Crystal X-ray Detector with Schottky Barrier for X-ray Imaging Application. *Gynecol. Endocrinol.* 36, 879–884. <https://doi.org/10.1021/acsaelm.9b00832>.
- He, Y., Petryk, M., Liu, Z., Chica, D.G., Hadar, I., Leak, C., Ke, W., Spanopoulos, I., Lin, W., Chung, D.Y., et al. (2020). CsPbBr<sub>3</sub> perovskite detectors with 1.4% energy resolution for high-energy  $\gamma$ -rays. *Nat. Photonics* 15, 36–42. <https://doi.org/10.1038/s41566-020-00727-1>.
- Feng, Y., Pan, L., Wei, H., Liu, Y., Ni, Z., Zhao, J., Rudd, P.N., Cao, L.R., and Huang, J. (2020). Low defects density CsPbBr<sub>3</sub> single crystals grown by an additive assisted method for gamma-ray detection. *J. Mater. Chem. C Mater.* 8, 11360–11368. <https://doi.org/10.1039/d0tc02706e>.
- Zhang, Y., Sun, R., Ou, X., Fu, K., Chen, Q., Ding, Y., Xu, L.J., Liu, L., Han, Y., Malko, A.V., et al. (2019). Metal Halide Perovskite Nanosheet for X-ray High-Resolution Scintillation Imaging Screens. *ACS Nano* 13, 2520–2525. <https://doi.org/10.1021/acsnano.8b09484>.
- Dirin, D.N., Cherniukh, I., Yakunin, S., Shynkarenko, Y., and Kovalenko, M.V. (2016). Solution-Grown CsPbBr<sub>3</sub> Perovskite Single Crystals for Photon Detection. *Chem. Mater.* 28, 8470–8474. <https://doi.org/10.1021/acs.chemmater.6b04298>.
- Dong, Q., Fang, Y., Shao, Y., Mulligan, P., Qiu, J., Cao, L., and Huang, J. (2015). Solar cells. Electron-hole diffusion lengths > 175  $\mu$ m in solution-grown CH<sub>3</sub>NH<sub>3</sub>PbI<sub>3</sub> single crystals. *Science* 347, 967–970. <https://doi.org/10.1126/science.1221048>.
- He, Y., Pan, W., Guo, C., Zhang, H., Wei, H., and Yang, B. (2021). 3D/2D Perovskite Single Crystals Heterojunction for Suppressed Ions Migration in Hard X-Ray Detection. *Adv. Funct. Mater.* 31. <https://doi.org/10.1002/adfm.202104880>.
- Thirimanne, H.M., Jayawardena, K.D.G.I., Parnell, A.J., Bandara, R.M.I., Karalasingam, A., Pani, S., Huedler, J.E., Lidzey, D.G., Tedde, S.F., Nisbet, A., et al. (2018). High sensitivity organic inorganic hybrid X-ray detectors with direct transduction and broadband response. *Nat. Commun.* 9, 2926. <https://doi.org/10.1038/s41467-018-05301-6>.
- Joglekar, S.G., Hammig, M.D., and Guo, L.J. (2019). High-Energy Photon Spectroscopy Using All Solution-Processed Heterojunctioned Surface-Modified Perovskite Single Crystals. *ACS Appl. Mater. Interfaces* 11, 33399–33408. <https://doi.org/10.1021/acsmi.9b09381>.
- Cao, M., Tian, J., Cai, Z., Peng, L., Yang, L., and Wei, D. (2016). Perovskite heterojunction based on CH<sub>3</sub>NH<sub>3</sub>PbBr<sub>3</sub> single crystal for high-sensitive self-powered photodetector. *Appl. Phys. Lett.* 109. <https://doi.org/10.1063/1.4971772>.
- Saidaminov, M.I., Haque, M.A., Savoie, M., Abdelhady, A.L., Cho, N., Dursun, I., Buttner, U., Alarousu, E., Wu, T., and Bakr, O.M. (2016). Perovskite Photodetectors Operating in Both Narrowband and Broadband Regimes. *Adv. Mater.* 28, 8144–8149. <https://doi.org/10.1002/adma.201601235>.
- Zhong, Y., Sisto, T.J., Zhang, B., Miyata, K., Zhu, X.Y., Steigerwald, M.L., Ng, F., and Nuckolls, C. (2017). Helical Nanoribbons for Ultra-Narrowband Photodetectors. *J. Am. Chem. Soc.* 139, 5644–5647. <https://doi.org/10.1021/jacs.6b13089>.
- Lin, Q., Armin, A., Burn, P.L., and Meredith, P. (2015). Filterless narrowband visible photodetectors. *Nat. Photonics* 9, 687–694. <https://doi.org/10.1038/nphoton.2015.175>.
- Fang, Y., Dong, Q., Shao, Y., Yuan, Y., and Huang, J. (2015). Highly narrowband perovskite single-crystal photodetectors enabled by surface-charge recombination. *Nat. Photonics* 9, 679–686. <https://doi.org/10.1038/nphoton.2015.156>.
- Wei, H., Fang, Y., Mulligan, P., Chuirazzi, W., Fang, H.-H., Wang, C., Ecker, B.R., Gao, Y.,

- Loi, M.A., Cao, L., and Huang, J. (2016). Sensitive X-ray detectors made of methylammonium lead tribromide perovskite single crystals. *Nat. Photonics* 10, 333–339. <https://doi.org/10.1038/nphoton.2016.41>.
21. An, Q., Yao, W., Wu, J., Pan, L., and Wang, X. (2020). Performance of Perovskite CsPbBr<sub>3</sub> Single Crystal Detector for Gamma-Ray Detection. *Soc. Work. Publ. Health* 35, 443–455. <https://doi.org/10.1109/tns.2020.2964306>.
  22. Du, Y., Xin, C., Huang, W., Shi, B., Ding, Y., Wei, C., Zhao, Y., Li, Y., and Zhang, X. (2018). Polymeric Surface Modification of NiOx-Based Inverted Planar Perovskite Solar Cells with Enhanced Performance. *ACS Sustain. Chem. Eng.* 6, 16806–16812. <https://doi.org/10.1021/acssuschemeng.8b04078>.
  23. He, R., Wang, W., Yi, Z., Lang, F., Chen, C., Luo, J., Zhu, J., Thiesbrummel, J., Shah, S., Wei, K., et al. (2023). All-perovskite tandem 1 cm<sup>2</sup> cells with improved interface quality. *Nature* 618, 80–86. <https://doi.org/10.1038/s41586-023-05992-y>.
  24. Shan, C., Zhao, M., Jiang, D., Li, Q., Li, M., Zhou, X., Duan, Y., Wang, N., and Deng, R. (2019). Improved responsivity performance of ZnO film ultraviolet photodetectors by vertical arrays ZnO nanowires with light trapping effect. *Nanotechnology* 30, 305703. <https://doi.org/10.1088/1361-6528/ab0ee5>.
  25. Pan, J., Chen, J., Huang, Q., Khan, Q., Liu, X., Tao, Z., Zhang, Z., Lei, W., and Nathan, A. (2016). Size Tunable ZnO Nanoparticles To Enhance Electron Injection in Solution Processed QLEDs. *ACS Photonics* 3, 215–222. <https://doi.org/10.1021/acsp Photonics.5b00267>.
  26. Wang, X., Xu, Y., Pan, Y., Li, Y., Xu, J., Chen, J., Wu, J., Li, Q., Zhang, X., Zhao, Z., et al. (2021). Low-noise X-ray PIN photodiodes made of perovskite single crystals by solution-processed dopant incorporated epitaxial growth. *Nano Energy* 89, 106311. <https://doi.org/10.1016/j.nanoen.2021.106311>.
  27. Wang, X., Li, Y., Xu, Y., Pan, Y., Zhu, C., Zhu, D., Wu, Y., Li, G., Zhang, Q., Li, Q., et al. (2020). Solution-Processed Halide Perovskite Single Crystals with Intrinsic Compositional Gradients for X-ray Detection. *Chem. Mater.* 32, 4973–4983. <https://doi.org/10.1021/acs.chemmater.9b05000>.
  28. Li, Y.-W., Wang, X., Li, G.-W., Wu, Y., Pan, Y.-Z., Xu, Y.-B., Chen, J., and Lei, W. (2020). Fast Liquid Phase Epitaxial Growth for Perovskite Single Crystals. *Chin. Phys. Lett.* 37, 018101. <https://doi.org/10.1088/0256-307x/37/1/018101>.
  29. Wang, X., Pan, Y., Xu, Y., Zhao, J., Li, Y., Li, Q., Chen, J., Zhao, Z., Zhang, X., Elemike, E.E., et al. (2022). High Spectral-Rejection-Ratio Narrowband Photodetectors Based on Perovskite Heterojunctions. *Adv. Electron. Mater.* 8. <https://doi.org/10.1002/aeml.202200178>.
  30. Ulatowski, A.M., Wright, A.D., Wenger, B., Buizza, L.R.V., Motti, S.G., Eggimann, H.J., Savill, K.J., Borchert, J., Snaith, H.J., Johnston, M.B., and Herz, L.M. (2020). Charge-Carrier Trapping Dynamics in Bismuth-Doped Thin Films of MAPbBr<sub>3</sub> Perovskite. *J. Phys. Chem. Lett.* 11, 3681–3688. <https://doi.org/10.1021/acs.jpcclett.0c01048>.
  31. Meng, R., Wu, G., Zhou, J., Zhou, H., Fang, H., Loi, M.A., and Zhang, Y. (2019). Understanding the Impact of Bismuth Heterovalent Doping on the Structural and Photophysical Properties of CH<sub>3</sub>NH<sub>3</sub>PbBr<sub>3</sub> Halide Perovskite Crystals with Near-IR Photoluminescence. *Chemistry* 25, 5480–5488. <https://doi.org/10.1002/chem.201805370>.
  32. Siegler, T.D., Zhang, Y., Dolocan, A., Reimnitz, L.C., Torabi, A., Abney, M.K., Choi, J., Cossio, G., Houck, D.W., Yu, E.T., et al. (2019). Addition of Monovalent Silver Cations to CH<sub>3</sub>NH<sub>3</sub>PbBr<sub>3</sub> Produces Crystallographically Oriented Perovskite Thin Films. *ACS Appl. Energy Mater.* 2, 6087–6096. <https://doi.org/10.1021/acsaem.9b01298>.
  33. Hettiarachchi, C., Birowosuto, M.D., Nguyen, T.H., Ahmad, R., Pita, K., Mathews, N., and Dang, C. (2018). Solution grown double heterostructure on a large hybrid halide perovskite crystal. *CrystEngComm* 20, 6653–6661. <https://doi.org/10.1039/c8ce01298a>.
  34. Zhang, Y., Lu, D., Gao, M., Lai, M., Lin, J., Lei, T., Lin, Z., Quan, L.N., and Yang, P. (2019). Quantitative imaging of anion exchange kinetics in halide perovskites. *Proc. Natl. Acad. Sci. USA* 116, 12648–12653. <https://doi.org/10.1073/pnas.1903448116>.
  35. Pan, D., Fu, Y., Chen, J., Czech, K.J., Wright, J.C., and Jin, S. (2018). Visualization and Studies of Ion-Diffusion Kinetics in Cesium Lead Bromide Perovskite Nanowires. *Nano Lett.* 18, 1807–1813. <https://doi.org/10.1021/acs.nanolett.7b05023>.
  36. Son, J.Y., Kim, B.G., Kim, C.H., and Cho, J.H. (2004). Writing polarization bits on the multiferroic BiMnO<sub>3</sub> thin film using Kelvin probe force microscope. *Appl. Phys. Lett.* 84, 4971–4973.
  37. Wei, H., DeSantis, D., Wei, W., Deng, Y., Guo, D., Savenije, T.J., Cao, L., and Huang, J. (2017). Dopant compensation in alloyed CH<sub>3</sub>NH<sub>3</sub>PbBr<sub>3</sub>-xCl<sub>x</sub> perovskite single crystals for gamma-ray spectroscopy. *Nat. Mater.* 16, 826–833. <https://doi.org/10.1038/nmat4927>.
  38. Zhao, L., Zhou, Y., Shi, Z., Ni, Z., Wang, M., Liu, Y., and Huang, J. (2023). High-yield growth of FACsPbBr<sub>3</sub> single crystals with low defect density from mixed solvents for gamma-ray spectroscopy. *Nat. Photonics* 17, 315–323. <https://doi.org/10.1038/s41566-023-01154-8>.

## STAR★METHODS

## KEY RESOURCES TABLE

REAGENT or RESOURCE	SOURCE	IDENTIFIER
Chemicals, peptides, and recombinant proteins		
PbBr <sub>2</sub>	Sigma Aldrich	10031-22-8
PbCl <sub>2</sub>	Sigma Aldrich	7758-95-4
CH <sub>3</sub> NH <sub>3</sub> Br	Sigma Aldrich	6876-37-5
CH <sub>3</sub> NH <sub>3</sub> Cl	Sigma Aldrich	593-51-1
BiBr <sub>3</sub>	Sigma Aldrich	7787-58-8
AgBr	Sigma Aldrich	7785-23-1
BiCl <sub>3</sub>	Sigma Aldrich	7787-60-2

## RESOURCE AVAILABILITY

## Lead contact

Further information and requests for resources and materials should be directed to and will be fulfilled by the lead contact, Xin Wang ([xinw@seu.edu.cn](mailto:xinw@seu.edu.cn)).

## Materials availability

This study did not generate new unique reagents.

## Data and code availability

Data reported in this paper will be shared by the [lead contact](#) upon request.

This paper does not report original code.

Any additional information required to reanalyze the data reported in this paper is available from the [lead contact](#) upon request.

## METHODS DETAILS

## Growth of the cascade HLPSC PIN photodiodes

Bidoped MAPbCl<sub>3</sub> HLPSCs were grown through inverse temperature crystallization as substrates. Then, MAPbCl<sub>3</sub>, MAPbBr<sub>2.5</sub>Cl<sub>0.5</sub>, MAPbBr<sub>3</sub>, and Ag-doped MAPbBr<sub>3</sub> through epitaxial growth in steps. After the growth of Ag-doped MAPbBr<sub>3</sub>, diamond wire was used to cut the cascade HLPSCs to remove the useless parts. Then, diamond powder disperse in isopropanol were used as polishing fluid to polish the faces of the cascade HLPSCs. Then, two Au electrodes were deposited on the faces of Bidoped MAPbCl<sub>3</sub> and Ag-doped MAPbBr<sub>3</sub> with vacuum degree 10<sup>-3</sup>Pa.

## Characterization of the HLPSC and photodiodes

X-ray diffraction (XRD) patterns were obtained using an X'TRA system with a Cu target (Switzerland). Scanning electron microscopy (SEM) images were obtained using a Quanta 200 FEI microscope. The samples for high resolution transmission electron microscopy (HR-TEM) characterization were prepared by focus ion beam (Helios 5 CX). The HR-TEM is characterized with TEM (JEM-200CX, JAPAN) with a high voltage 220 kV. To ensure that the detectors receive enough X-ray photons in EDX, the counts per second is controlled nearly 1200 in the experiments. The Kelvin probe force microscopy (KPFM) probe station (Multimode-8-AM, USA) was used to measure the contact potential difference (CPD). Dark current density-voltage (J-V) characteristics were measured using a Keithley 4200 semiconductor analyzer (USA).

## Experiments of the gamma-ray photodiodes

CdTe single crystal and CdZnTe single crystal were bought From Acrorad, Japan and eV, USA, respectively. The charges preamplifier is based on CR-110 (rev2.1) from CREMAT (USA) and we design the peripheral circuit. And the shaping amplifiers including CR-200(1 μs, 2 μs, 4 μs, and 8 μs) and baseline restorer CR-210 are brought from CREMAT (USA). The high voltage source (0–1500 V) is brought from Dongwen high voltage (China). And the multiple-channel analyzer (APG7300A) is brought from AP.Co (Japan).

## QUANTIFICATION AND STATISTICAL ANALYSIS

No statistical analysis is used.